



UNIVERSITY OF LEEDS

This is a repository copy of *A human ear-inspired ultrasonic transducer (HEUT) for 3D localization of sub-wavelength scatterers*.

White Rose Research Online URL for this paper:

<https://eprints.whiterose.ac.uk/203391/>

Version: Accepted Version

---

**Article:**

Nie, L. [orcid.org/0000-0002-5796-907X](https://orcid.org/0000-0002-5796-907X), Toulemonde, M. [orcid.org/0000-0002-3191-8020](https://orcid.org/0000-0002-3191-8020), Tang, M.-X. [orcid.org/0000-0001-7686-425X](https://orcid.org/0000-0001-7686-425X) et al. (2 more authors) (2023) A human ear-inspired ultrasonic transducer (HEUT) for 3D localization of sub-wavelength scatterers. *Applied Physics Letters*, 123 (8). 082203. ISSN 0003-6951

<https://doi.org/10.1063/5.0152029>

---

© 2023 Author(s). Published under an exclusive license by AIP Publishing. This is an author produced version of an article published in *Applied Physics Letters*. Uploaded in accordance with the publisher's self-archiving policy.

**Reuse**

Items deposited in White Rose Research Online are protected by copyright, with all rights reserved unless indicated otherwise. They may be downloaded and/or printed for private study, or other acts as permitted by national copyright laws. The publisher or other rights holders may allow further reproduction and re-use of the full text version. This is indicated by the licence information on the White Rose Research Online record for the item.

**Takedown**

If you consider content in White Rose Research Online to be in breach of UK law, please notify us by emailing [eprints@whiterose.ac.uk](mailto:eprints@whiterose.ac.uk) including the URL of the record and the reason for the withdrawal request.



[eprints@whiterose.ac.uk](mailto:eprints@whiterose.ac.uk)  
<https://eprints.whiterose.ac.uk/>

# **A Human Ear-inspired Ultrasonic Transducer (HEUT) for 3-D Localization of Sub-wavelength Scatterers**

**Luzhen Nie<sup>1</sup>, Matthieu Toulemonde<sup>2</sup>, Meng-Xing Tang<sup>2</sup>, Steven Freear<sup>1</sup>, and Sevan Harput<sup>3\*</sup>**

<sup>1</sup>School of Electronic and Electrical Engineering, University of Leeds, Leeds, U.K.

<sup>2</sup>Department of Bioengineering, Imperial College London, London, U.K.

<sup>3</sup>Division of Electrical and Electronic Engineering, London South Bank University, London, U.K.

\*E-mail: harputs@lsbu.ac.uk

## **ABSTRACT**

The proposed technology aims to enable 3-D localization of scatterers using single-element ultrasonic transducers, which are traditionally limited to 1-D measurements. This is achieved by designing a bespoke acoustic lens with a spiral-shaped pattern similar to the human outer ear, a shape that has evolved for sound source localization. This lens breaks the surface symmetry of the transducer, allowing ultrasonic waves arriving from different directions to be encoded in a certain way that can later be decoded to extract directional information. By employing the mechanism of spatial-encoding of the received signals and decoding via signal processing, the location of sub-wavelength scatterers can be detected in 3-D with a single measurement for sparsely distributed scatterers. The proposed technology is first verified through a simulation study, and then 3-D printed acoustic lenses are used to demonstrate the 3-D encoding functionality of the Human Ear-inspired Ultrasonic Transducer (HEUT) experimentally. A framework is created to localize scatterers in 3-D by processing received signals acquired by a HEUT prototype. With this technology, a single transducer can obtain multi-dimensional information with a single pulse-echo measurement, reducing the number of elements required for performing 3-D ultrasound localization. The proposed spatial-encoding and –decoding technology can be applied to other wave-based imaging methods to develop affordable, practical and compact sensing devices.

Simpler, more affordable, compact, and energy-efficient 3-D acoustic localization systems are desired for use in a wide range of non-destructive testing (NDT) and underwater search and survey applications, such as autonomous underwater vehicles (AUVs) and handheld sonar devices [1, 2, 3]. However, the implementation of such a 3-D system typically employs either multiple elements/channels or multiple measurements with cumbersome mechanical rotating units to acquire 3-D information [4, 5, 6, 7, 8], resulting in high hardware complexity, cost and dimensions. In this study, an acoustic lens is designed to enable spatial-encoding of the received signal, which can achieve 3-D underwater localization with a single measurement performed by a single element ultrasound transducer without any moving parts, promising a hardware efficient system that could find applications in NDT, AUVs and handheld sonar devices.

Conventionally, 3-D localization is not possible by only using a single element ultrasound transducer. Consider three scenarios, where a scatterer is relocated with the identical radial distance ( $r$ ) but different polar ( $\theta$ ) and azimuthal ( $\phi$ ) angles as schematically illustrated in Figure 1. By definition, the A-mode method only uses the envelope of the received signal to find the radial distance of the scatterer through a time-of-flight measurement. Therefore, A-mode scans performed for all three scenarios will result in the same 1-D information, radial distance. Although the envelopes of the signals are almost the same, there are considerable differences between the received echoes in scenario 1 and 2, or scenario 1 and 3, as shown in Figure 1. The differences are due to the spatial filtering effect of the transducer, which modifies the received echo depending on the angle of incidence. By using the phase of the signal as explained in [9], scatterers can be localized in 2-D, ( $r, \theta$ ), where scenario 1 and 2, or scenario 1 and 3 can be differentiated, but it is not possible to differentiate scenario 2 from scenario 3 as the received signal is identical for both cases. However, when the transducer surface symmetry is broken, the ultrasound waves arriving from different azimuthal directions will be distorted in a distinct manner.

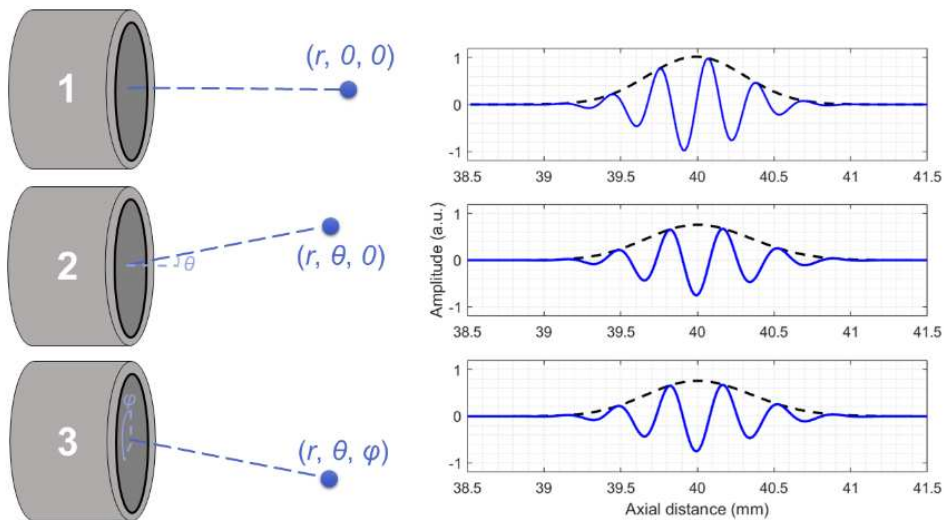


**Fig. 1.** Three different scenarios are schematically illustrated to highlight the importance of breaking the surface symmetry. (Left) Illustration of the transducer and scatterer positions. For each scenario, the scatterer is relocated to a different spherical coordinate with respect to the center of the transducer. (Right) The received signals and their envelopes are shown in blue and dashed black lines, respectively. It is not possible to differentiate between scenario 2 and 3, since the transducer's aperture is symmetric and a relocation of the scatterer with different azimuths ( $\phi$ ) does not change the received signal.

To break the surface symmetry and achieve 3-D localization, we developed an ultrasound transducer with an acoustic lens inspired by the human ear. The asymmetry of the human outer ear, pinna, plays an essential role for localization in hearing [10]. Researchers have shown that the pinna performs a location-dependent filtering of sounds, providing spectral cues that help to determine the direction of a sound source [11]. While most humans rely on both the shape of the pinna and the differential information provided by two ears for sound source localization, monaural listeners are able to localize sound source elevation and azimuth based on spectral cues alone [12]. To replicate this spatial filtering capability of the pinna, we considered implementing different features of the outer ear, such as *helix*, *antihelix*, *concha*, *tragus* and *lobule*. However, Guezenoc and Séguier demonstrated that *helix* and *antihelix* are the main components of the human ear based on their principle component analysis of a wide dataset of human ear shapes [13]. Similarly, Chen and Bhanu showed that the *helix* and *antihelix* are the most significant features of the outer ear used for 3-D ear recognition [14]. By using this phenomenon, we propose a Human Ear-inspired Ultrasonic Transducer (HEUT) in this study, which is based on the *helix* and *antihelix* of the pinna to improve the localization capability of single

element transducers. With a single acquisition, HEUT can identify the locations of sub-wavelength scatterers in 3-D.

For the acoustic lens design, the *helix* and *antihelix* features of the outer ear were implemented by a spiral-shaped mask to break the transducer surface symmetry. The spiral-shaped mask in a form of air filled channels was embedded in a 3D printed lens, which was then attached to a single element ultrasound transducer to form a HEUT prototype, as shown in Figure 2.

The *helix* was first designed with a single spiral, and a second spiral was added to implement the *antihelix* feature (see Figure 2 top-left). A single element transducer of 6-mm diameter working at 2.4 MHz was chosen for both simulations and experiments. Both the thickness of the spirals and the separation angle between the two spirals were designed by using Field II [15, 16], and the values of a quarter of the wavelength and  $90^\circ$  were adopted. During transmission, the acoustic lens had a negligible effect on the transmit beam profile in the far field. During reception, the dual spiral-shaped mask encoded the received signal in a certain way that was possible to decode and extract directional information. Field II utilizes the Tupholme-Stepanishen method [15] to simulate linear ultrasound transducer fields and ultrasound pulse echo. It solves the simulation analytically, defining the transducer aperture with rigid-baffle boundary conditions. Besides the transducer's shape and aperture size, it requires the definitions of the excitation signal, electromechanical pulse response, and scatterer locations along with their intensities. In the simulations, a one-cycle sinusoid at 2.4 MHz was adopted as the excitation signal, and a Gaussian pulse with a center frequency of 2.4 MHz and a 60% fractional bandwidth was used as the electromechanical pulse response. Arbitrary units were used in both the simulations and the presentation of simulation results. Further details about the acoustic lens design and simulations are explained in the supplementary material. Please refer to the statement at the end of the manuscript for code availability.

The lenses were then additively manufactured with a Form 3L SLA printer (Formlabs, MA, USA) with ELEGOO ABS-like photopolymer resin. A solid cylinder block of 0.6 mm thickness and 9.6 mm diameter was made as the empty lens for reference. The designed lenses had the identical cylinder shape but with single or dual spiral-shaped grooves (air channels) on one side to create the surface asymmetry as shown in Figure 2. The air channels had a width and depth of 250  $\mu\text{m}$ , corresponding to  $\lambda/4$  at a frequency of 2.4 MHz for a sound speed of 2400 m/s through the lens material. The acoustic attenuation of the lens material was measured to be 11.4 dB/cm/MHz at 2.4 MHz, and the density was 1.2 g/cm<sup>3</sup>, resulting in an acoustic impedance of 2.88 MPa·s/m. In experiments, acoustic lenses were placed in contact with the transducer to block part of the transducer's active surface using spiral-shaped masks with acoustically opaque air channels.

The ultrasound setup consisted of a single element transducer working at 2.4 MHz (Olympus Scientific Solutions Americas Inc., MA), acoustic lenses and an Ultrasound Array Research Platform (UARP) [17, 18, 19], which was used to measure directional responses (spatial encoding) of the acoustic lenses. A 200- $\mu\text{m}$  wire was used as the point scatterer. A one-cycle sinusoid at 2.4 MHz was used as the transmit waveform. The transducer was moved by a motorized translation stage (MTS50C-Z8, Thorlabs Ltd., U.K.). More details of the experimental setup are provided in the supplementary material.

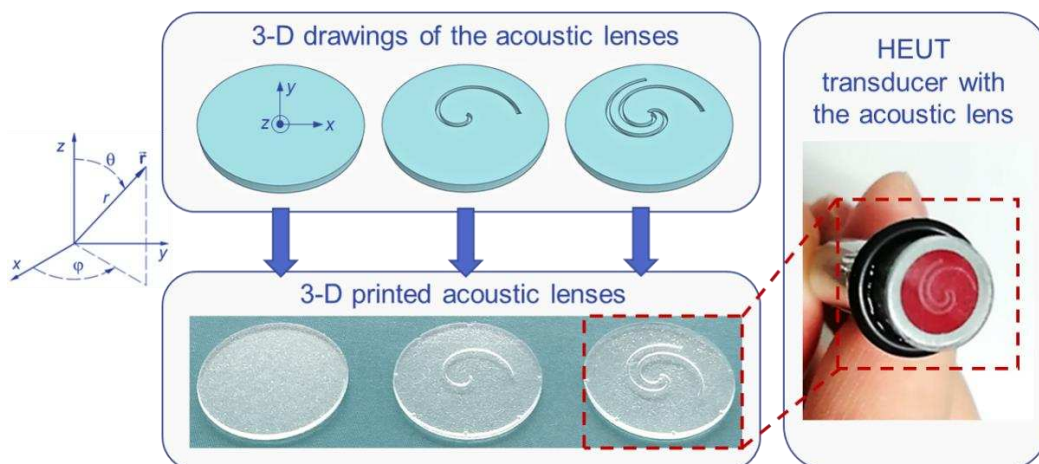


**Fig. 2.** (Top-left) 3-D drawing of the acoustic lenses with no mask (empty lens), a single spiral- and dual spiral-shaped mask. (Bottom-left) Photograph of the 3-D printed acoustic lenses. (Right) Photograph of the HEUT prototype transducer with an acoustic lens.

Simulations were first performed to compare the performance of a control measurement without a mask, and measurements with a single spiral- and dual spiral-shaped mask. Figure 3a shows the received signals from 7 different scatterers located at the following spherical ( $r, \theta, \varphi$ ) coordinates;  $r = 40$  mm and  $\varphi = 90^\circ$  with a varying polar angle of  $\theta = 0^\circ, 0.72^\circ, 1.43^\circ, 2.15^\circ, 2.87^\circ, 3.58^\circ$  and  $4.3^\circ$ . These locations corresponded to lateral translation of a scatterer in x-direction as  $x = 0, 0.5, 1.0, 1.5, 2.0, 2.5$  and  $3.0$  mm (see Figure 2 or Figure S1 in the supplementary material for axes). The purpose of this simulation was to show that the spiral-shaped masks can be used to detect the polar angle of the scatterer,  $\theta$  [9].

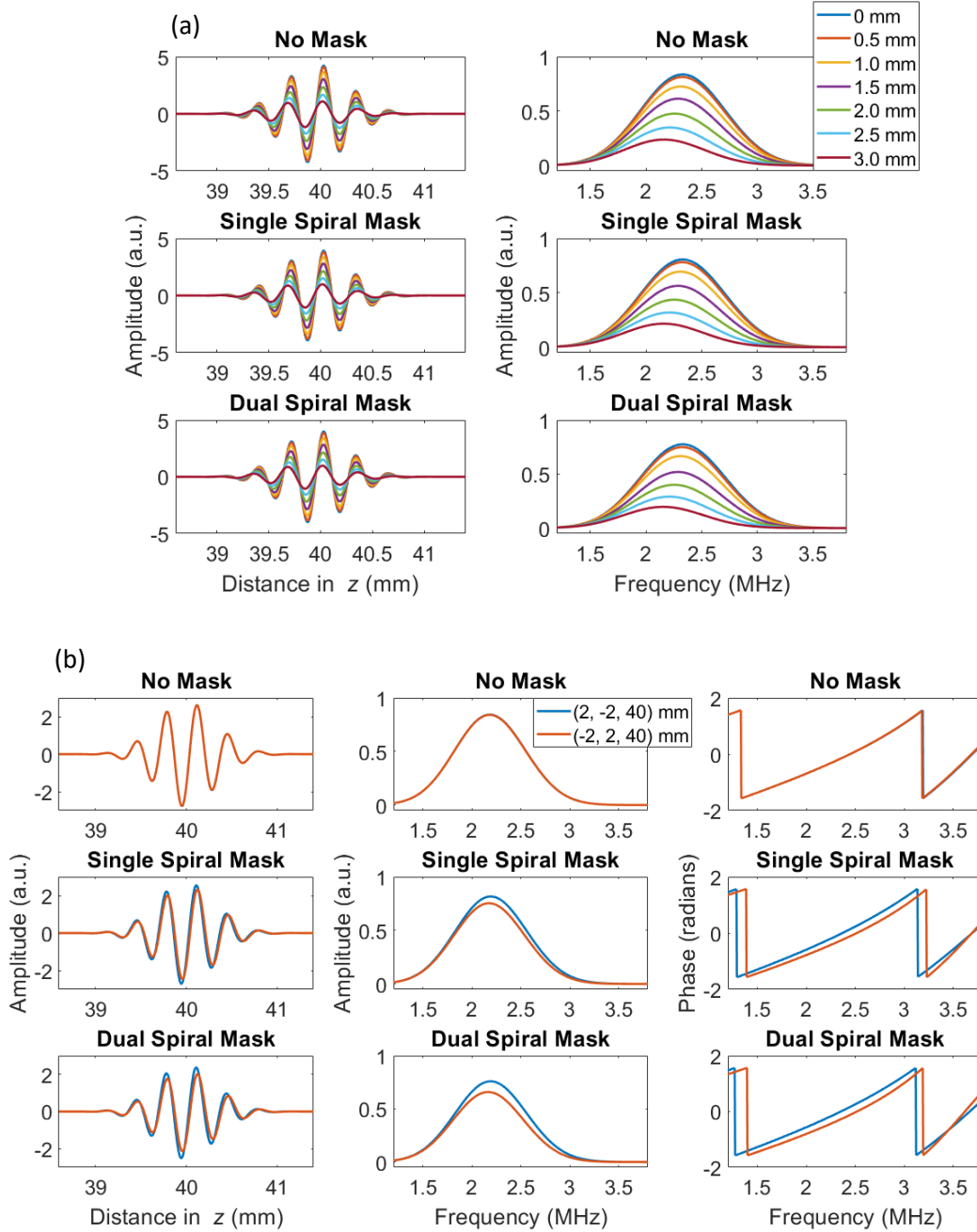


**Fig. 3. (a)** (Left) Time domain signals for 7 simulated scatterers, (right) corresponding spectral amplitudes of the received signals for an empty lens, a lens with a single spiral- and dual spiral-shaped mask, respectively. **(b)** Time and frequency domain comparison of the simulated received signals for scatterers located at (2, -2, 40) and (-2, 2, 40) mm for an empty lens, a lens with a single spiral- and dual spiral-shaped mask.

Figure 3a (right column) shows the spatial encoding of the received signal as a result of lateral translation of the scatterer, which effectively changes with the angle of incidence,  $\theta$ . For all three simulations with or without a mask, the spectral peak shifts as a function of the scatterer angle,  $\theta$ . For the dual spiral-shaped mask, the angle  $\theta$  of the scatterer could be determined with Equation (1), where  $f_p$  is the frequency peak in MHz and  $\theta$  is the polar angle of the scatterer in degrees;

$$f_p = 2.331 - 0.009\theta^2 \quad (1)$$

Equation (1) was formulated by fitting a polynomial to the peak frequency response and it can be used to estimate the polar angle with an average error of  $0.04^\circ$  and a maximum error of  $0.19^\circ$ , which was validated for  $0^\circ \leq \theta \leq 5^\circ$  and  $0^\circ \leq \varphi < 360^\circ$  with simulations.

To reproduce the problem described in Figure 1, another simulation was performed with two mirrored scatterers located at the following spherical  $(r, \theta, \varphi)$  coordinates;  $(40.1 \text{ mm}, 4.05^\circ, 135^\circ)$  and  $(40.1 \text{ mm}, 4.05^\circ, 315^\circ)$ , which corresponded to  $(2, -2, 40)$  and  $(-2, 2, 40)$  mm in x-y-z coordinates. Figure 3b shows the received signals from these scatterers, where the empty mask cannot achieve 3-D encoding as the mirrored scatterers located at  $(2, -2, 40)$  and  $(-2, 2, 40)$  mm provide the identical signal due to the symmetrical aperture of the transducer.

Both the single spiral- and dual spiral-shaped masks break this symmetry and could be used to differentiate these scatterers. The azimuthal angle of the scatterer could be determined by finding the zero-crossing of the signal's phase shown in Figure 3b (right bottom for the dual spiral-shaped mask), where the phase response of the scatterer located at  $\varphi = 135^\circ$  has a zero-crossing at 2.35 MHz and for  $\varphi = 315^\circ$ , it is 2.56 MHz. The zero-crossing point could be used to unambiguously locate the scatterers since it changes with the azimuthal angle as verified in simulations. For the dual spiral-shaped mask, the azimuthal angle of the scatterer could be determined with Equation (2), where  $f_{zc}$  is the zero-crossing frequency of the signal's phase in MHz and  $\varphi$  is the angle in degrees;

$$f_{zc} = 2.35 + 9 \times 10^{-6}(\varphi - 125)^2 \quad (2)$$

Equation (2) can be used to estimate the azimuthal angle with an average and maximum error of  $11.1^\circ$  and  $17.2^\circ$ , as validated for the simulations performed at  $\theta = 4.05^\circ$  and  $0^\circ \leq \varphi < 360^\circ$ .

In another simulation, the localization capability of the dual spiral-shaped mask was further tested using 25 random scatterers with a uniform distribution. These scatterers were within the main transmit beam; between 15 and 50 mm in z-direction and up to 3 mm away from the main axis in x- and y-directions.

A localization framework consisting of three steps was developed to determine the location of scatterers in spherical coordinates.

- 1- Measure the time of flight of the received signal to calculate  $r$ . This approach is the same as the A-mode scan.
- 2- Measure the location of the received signal's spectral peak to estimate  $\theta$  using an equation similar to Equation (1), which is recalculated at each axial depth.
- 3- Measure the zero-crossing point of the received signal's phase response to estimate  $\varphi$  using an equation similar to Equation (2), which is recalculated at each axial depth.

The reason for recalculating Equation (1) and Equation (2) is due to the attenuation, where the quadratic part of the equations stayed the same but the offset frequency changed by depth.

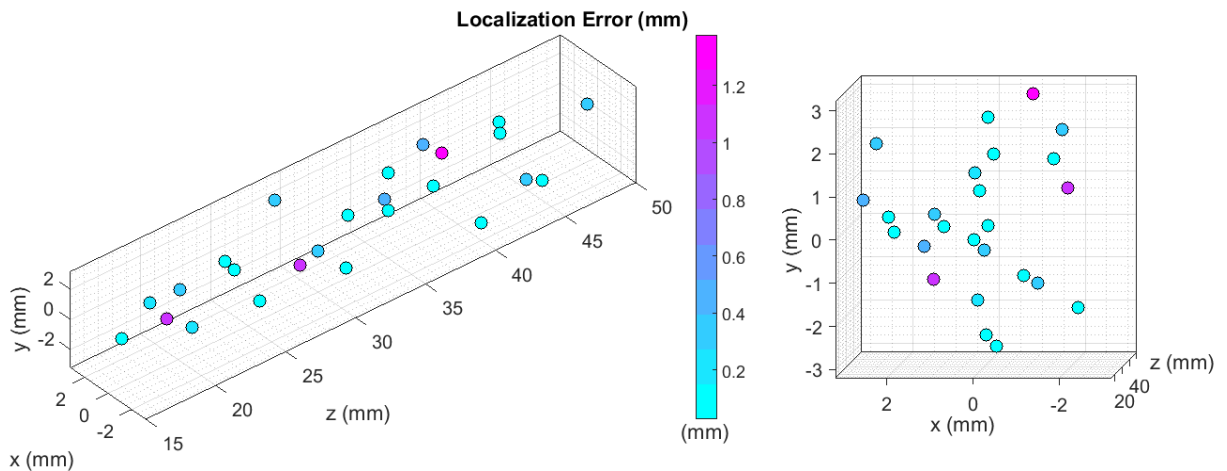


**Fig. 4.** Localization errors for 25 randomly simulated scatterers within the x-y-z Cartesian coordinates of  $(-3:3, -3:3, 15:50)$  mm. Left and right figures are the same scatterers plotted from different viewing angles for better visualization. Each scatterer is plotted at their exact location and color-coded according to their 3-D localization error.

The localization errors for the 25 randomly distributed scatterers generated within the x-y-z Cartesian coordinates of (-3:3, -3:3, 15:50) mm were calculated, where the error was the Euclidian distance between the correct and predicted 3-D positions. Figure 4 shows the corresponding localization errors for each randomly distributed scatterer, which is  $0.30 \pm 0.36$  mm for HEUT with the dual spiral-shaped mask, compared to  $1.81 \pm 0.90$  mm for a traditional A-scan mode.

First set of experimental measurements were performed to verify the simulations presented in Figure 3a using a point scatterer placed at (0, 0, 40) mm. The transducer was then moved along the x-direction with a distance up to 3 mm at increments of 0.5 mm, where Figure 5a shows the corresponding results. Note that the radial distance is changing between 40 and 40.22 mm due to the limitation of the translation stage.

The spatial filtering effect of the single-element transducer is observable in Figure 5a, where the received pressure field varies in both the time and frequency domains for a scatterer at different lateral locations. As shown in Figure 5a, 2-D localization could be unambiguously performed by finding the shift in the frequency domain, similar to the simulation study as shown in Figure 3a. The angular detection equation now becomes the following due to experimental nuances:

$$f_p = 2.239 - 0.006\theta^2 \quad (3)$$

Equation (3) could be used to estimate the polar angle with an average error of  $0.25^\circ$  and an outlier error value of  $0.89^\circ$ .

When the lenses are placed in front of the transducer, the received waveforms in the time domain have tails due to reverberations within the lens as shown in Figure 5a (left column). Correspondingly, a secondary peak at around 3 MHz is seen in Figure 5a (right column). This is one of the main differences between the simulations and experiments, where an ideal lens can be implemented in simulations without generating any reverberations. However, the proposed method can identify the location of a sub-wavelength scatterer even in the presence of reverberations.

Second set of experimental measurements were performed with scatterers located at (2, -2, 40) mm and (-2, 2, 40) mm in order to demonstrate the functionality of the acoustic lens to solve the 3-D localization problem described in Figure 1 and simulated in Figure 3b. Figure 5b shows the temporal waveforms, their corresponding spectra and phase responses for measurements acquired using an empty lens, a lens with a single spiral- and dual spiral-shaped mask. The measurements with an empty lens are provided as control, which cannot achieve 3-D encoding as expected, where the received signals from mirrored scatterers are almost identical. The surface symmetry is not strongly broken with a single spiral-shaped lens in simulations, and additional experimental imperfections make the separation of these two mirrored scatterers difficult with this lens. In contrast, the lens with a dual spiral-shaped mask introduces more phase diversity, leading to a more effective encoding. The azimuthal angle of the scatterer, for the lens with a dual spiral-shaped mask, could be determined by finding the zero-crossing of the signal's phase shown in Figure 5b (right bottom), where the phase response of the scatterer located at  $\varphi = 135^\circ$  has a zero-crossing at 2.25 MHz, and for  $\varphi = 315^\circ$ , it is 2.52 MHz. The azimuthal angles of these two scatterers could be estimated with an error of  $13.5^\circ$  through a modified version of Equation (2), where the frequency offset is changed to 2.25 due to experimental nuances.

In this work, we adapted the *helix* and *antihelix* shape of the pinna to design an acoustic lens with a spiral-shaped mask, resulting in a spatial filter that was not only sensitive to changes in the polar angle of  $\theta$ , but also sensitive to the azimuthal angle of  $\varphi$ . This technology can localize smaller-than-wavelength scatterers when their echoes can be separated in the time domain. This proof-of-concept study validated the working principle of the HEUT prototype by combining a single element ultrasound transducer and bespoke acoustic lenses. The designed dual spiral mask achieved a 3-D localization accuracy better than half a wavelength (0.31 mm for 2.4 MHz in water) on average for a set of randomly distributed scatterers *in silico*. Experiments showed that it is possible to identify the scatterer location in 3-D, though decoding of the received signal is not a straightforward task. The decoding of the polar and azimuthal angles could be performed by using empirical formulas, which need re-calibration for each specific transducer and acoustic lens pair. In addition, the measurement hardware could also affect the decoding process and a re-calibration may be required. The burden of the calibration process could be eased with several ways, and the easiest way could be the generation of a self-calibration method or the design of an adaptive filter to compensate for variations in transducer-lens response. If the proposed method is widely adopted, then manufacturers can perform the calibration of their transducers with the acoustic lenses. Empirical formulas have been investigated as one of the possible ways to decode the polar and azimuthal angles for localization in 3-D. In the future work, the 3-D localization process could be automated by using artificial intelligence-based solutions, such as training a neural network that incorporates the transducer-to-transducer variations [20, 21], attenuation [22], multiple scattering [22] and phase aberrations [23, 24].

A circular single element ultrasound transducer of 6 mm diameter has been chosen in the current study, and the used frequency of 2.4 MHz is within the range of multi-beam forward-looking sonar systems [2]. These values are chosen for illustrative purposes in this proof-of-concept study and would vary depending on practical requirements. For a given single element ultrasound transducer, it is possible to determine its radiating beam pattern either analytically or numerically. The proposed method in this study is designed to operate within the far field of the transducer, where the beam profile is relatively uniform and well-behaved with limited amplitude and phase irregularities. For the circular single element transducer used in the current study, its near field

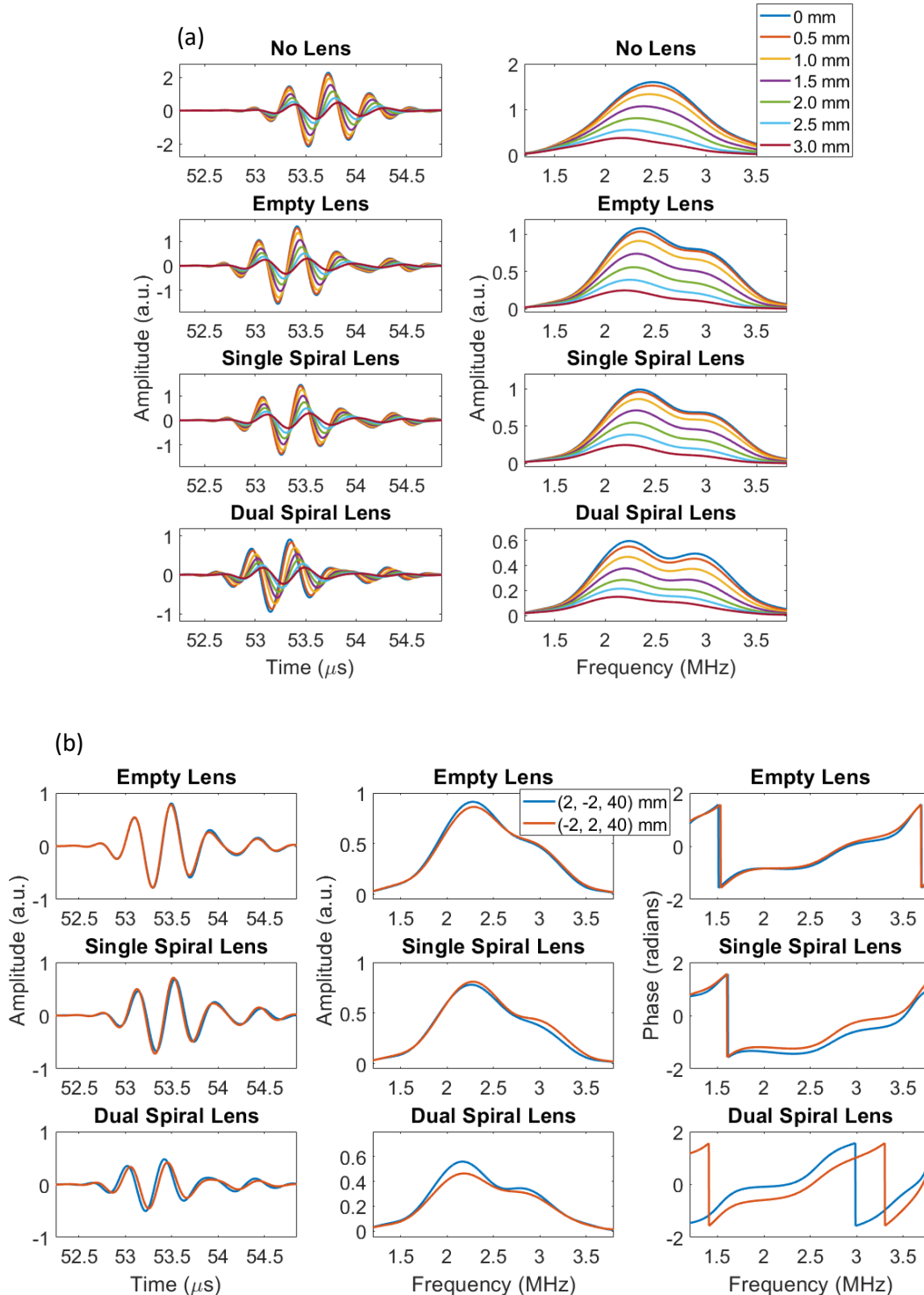


**Fig. 5. (a)** Received echoes for 7 scatterers located at varying lateral locations are shown (left) in the time domain with corresponding (right) spectral amplitudes. **(b)** Time and frequency domain comparison of the received signals from scatterers located at  $(2, -2, 40)$  and  $(-2, 2, 40)$  mm for an empty lens, a lens with a single spiral- and dual spiral-shaped mask.



length and beam divergence can be analytically calculated [25]. The beam divergence refers to the angle between one side of the beam and the central axis in the far field, where the transducer works more efficiently within this range. The localization range (or maximum detectable polar angle) achievable with the proposed method is constrained by the beam divergence, not by the design of the acoustic lens. For specific applications, it is possible to increase the beam divergence and, consequently, the localization range (or maximum detectable polar angle) by employing different means. This includes using a transducer with a smaller aperture size [25] or incorporating an additional divergent acoustic lens.

The HEUT technology does not require complex hardware, expensive electronics or moving parts, since the decoding of the direction information is performed in software using data acquired from a single channel. With a single element ultrasonic transducer, the proposed HEUT technology can be immediately applied for the detection of small defects in homogeneous materials or the localization of scatterers in hypo-echoic mediums. This technology can also be applied to handheld sonar devices and other wave-based imaging methods, such as Radar or Terahertz imaging. This technology can be a starting point to develop affordable, practical and compact sensing devices for new scientific applications.

## SUPPLEMENTARY MATERIAL

The supplementary material describes the bioinspiration and numerical simulations of the lens design, and the setup for experimental measurements.

## ACKNOWLEDGMENT

This work was funded by the Royal Society under grant RGS\R1\201012, and the U.K. EPSRC under grant EP/P023266/1.

## DATA AND CODE AVAILABILITY

The data and code that support the findings of this study are available from the corresponding author upon reasonable request.

## REFERENCES

- [1] A. Sahoo, S. K. Dwivedy, and P. S. Robi. "Advancements in the field of autonomous underwater vehicle." *Ocean Engineering* 181 (2019): 145-160.
- [2] Y. Wei, Y. Duan, and D. An. "Monitoring fish using imaging sonar: Capacity, challenges and future perspective." *Fish and Fisheries* 23, no. 6 (2022): 1347-1370.
- [3] S. Karabchevsky, K. David, O. Ben-Harush et al. "FPGA-based adaptive speckle suppression filter for underwater imaging sonar." *IEEE Journal of Oceanic Engineering* 36, no. 4 (2011): 646-657.
- [4] R. P. Hodges. *Underwater acoustics: Analysis, design and performance of sonar*. John Wiley & Sons, 2011.
- [5] Z. Lin, Y. Chen, X. Liu et al. "Optimized design for sparse arrays in 3-D imaging sonar systems based on perturbed Bayesian compressive sensing." *IEEE Sensors Journal* 20, no. 10 (2020): 5554-5565.
- [6] P. Kruizinga, P. van der Meulen, A. Fedjajevs et al. "Compressive 3-d ultrasound imaging using a single sensor," *Science Advances*, vol. 3, no. 12, pp. e1701423, 2017.
- [7] P. van der Meulen, P. Kruizinga, J. G. Bosch et al. "Coding mask design for single sensor ultrasound imaging," *IEEE Transactions on Computational Imaging*, vol. 6, pp. 358–373, 2019.
- [8] J. Janjic, P. Kruizinga, P. Van Der Meulen et al. "Structured ultrasound microscopy," *Applied Physics Letters*, vol. 112, no. 25, pp. 251901, 2018.
- [9] L. Nie, J. T. M. Moo, M. Toulemonde et al. "Localization of a Scatterer in 3D with a Single Measurement and Single Element Transducer", in *IEEE International Ultrasonics Symposium (IUS)*, 2020, pp. 1-4.
- [10] D. W. Batteau, "The role of the pinna in human localization", *Proc. R. Soc. Lond. B*, vol. 168, pp. 158–180, 1967.
- [11] V. Best and S. Carlile, "The role of high frequencies in speech localization", *The Journal of the Acoustical Society of America*, vol. 118, pp. 353-363, 2005.
- [12] M. M. Van Wanrooij, and A. J. V. Opstal, "Contribution of Head Shadow and Pinna Cues to Chronic Monaural Sound Localization", *Journal of Neuroscience*, vol. 24, no. 17, pp. 4163-4171, 2004.
- [13] C. Guezenoc, and R. Segquier. "A wide dataset of ear shapes and pinna-related transfer functions generated by random ear drawings", *Journal of the Acoustical Society of America*, vol. 147, no. 6, pp. 4087-4096, 2020.

- [14] H. Chen, and B. Bhanu. "Human Ear Recognition in 3D", IEEE Transactions on Pattern Analysis and Machine Intelligence, vol. 29, no. 4, pp. 718-737, 2007.
- [15] J. A. Jensen and N. B. Svendsen, "Calculation of pressure fields from arbitrarily shaped apodized and excited ultrasound transducers", IEEE Trans. Ultrason., Ferroelectr., Freq. Control, vol. 39, no. 2, pp. 262-267, 1992.
- [16] J. A. Jensen, "Field: A program for simulating ultrasound systems", 10th Nordicbaltic Conference On Biomedical Imaging, vol. 4, no. 1, pp. 351-353, 1996.
- [17] P. R. Smith, D. M. J. Cowell, B. Raiton et al. "Ultrasound array transmitter architecture with high timing resolution using embedded phase-locked loops," IEEE Trans. Ultrason., Ferroelectr., Freq. Control, vol. 59, no. 1, pp. 40-49, 2012.
- [18] D. M. J. Cowell, P. R. Smith, and S. Freear, "Phase-inversion-based selective harmonic elimination (PI-SHE) in multi-level switched-mode tone- and frequency- modulated excitation," IEEE Trans. Ultrason., Ferroelectr., Freq. Control, vol. 60, no. 6, pp. 1084-1097, 2013.
- [19] P. R. Smith, D. M. J. Cowell, and S. Freear, "Width-modulated squarewave pulses for ultrasound applications," IEEE Trans. Ultrason., Ferroelectr., Freq. Control, vol. 60, no. 11, pp. 2244-2256, 2013.
- [20] Y. Zhang, X. He, Z. Tian et al. "Multi-Needle Detection in 3D Ultrasound Images Using Unsupervised Order-Graph Regularized Sparse Dictionary Learning," in IEEE Transactions on Medical Imaging, vol. 39, no. 7, pp. 2302-2315, 2020.
- [21] R.J. van Sloun, O. Solomon, M. Bruce et al. "Super-Resolution Ultrasound Localization Microscopy Through Deep Learning," in IEEE Transactions on Medical Imaging, vol. 40, no. 3, pp. 829-839, 2021.
- [22] N. Blanken, J. M. Wolterink, H. Delingette et al. "Super-Resolved Microbubble Localization in Single-Channel Ultrasound RF Signals Using Deep Learning," in IEEE Transactions on Medical Imaging, vol. 41, no. 9, pp. 2532-2542, Sept. 2022.
- [23] D. Saha, U. Schmidt, Q. Zhang et al. "Practical sensorless aberration estimation for 3D microscopy with deep learning," Opt. Express 28, 29044-29053, 2020.
- [24] S. Jeon, W. Choi, B. Park et al. "A Deep Learning-Based Model That Reduces Speed of Sound Aberrations for Improved In Vivo Photoacoustic Imaging," in IEEE Transactions on Image Processing, vol. 30, pp. 8773-8784, 2021.
- [25] D. A. Christensen. Ultrasonic bioinstrumentation. John Wiley & Sons, 1988.

# Supplementary Material: A Human Ear-inspired Ultrasonic Transducer (HEUT) for 3-D Localization of Sub-wavelength Scatterers

Luzhen Nie, Matthieu Toulemonde, Meng-Xing Tang, Steven Freear, and Sevan Harput

## MOTIVATION FOR THE ACOUSTIC LENS DESIGN

The main purpose of the acoustic lens is to break the surface symmetry of the ultrasound transducer that has a circular aperture, for localizing scatterers in 3D. To achieve this, masks with different shapes are designed and embedded inside the acoustic lens as hollow grooves to block part of the received echoes and hence encode the received signal. When breaking the surface symmetry, the lens design focuses on minimizing the effects of the acoustic lens on transducer's transmit beam pattern in the far field and maximizing the spatial-encoding on receiving as explained below.

## BIOINSPIRATION

The design of the acoustic lens is inspired from the human ear, which has a 3-D sound localization capability. However, the human perceptual model for 3-D sound source localization is complex. Humans use a combination of different phenomena for sound localization by comparing the difference between sound waves received from both ears and by using the directional response provided by each ear [1, 2]. A head-related transfer function (HRTF) combines the interaural time difference (ITD), which is due to the distance between ears, and interaural intensity difference (IID), which is caused by the acoustic shadow generated by the human head, to model the sound waves received by each ear. For most cases, the differential information generated by using the HRTF may be sufficient for source localization. Although the HRTF model is widely accepted, it cannot represent the functionality provided by a single ear. The pinna provides a unique spatial filtering effect that the brain can decode the spatially filtered echoes and use them for sound localization [3]. This is possible thanks to its special shape, which is asymmetrical in both horizontal and vertical directions. The binaural listeners, who use both ears, combine the HRTF and pinna's filtering effect to locate a particular sound source in space. However, monaural listeners, who use only one ear, purely rely on the shape of the pinna for sound source localization, as they cannot utilize the stereo information provided by the HRTF [1].

The principle of HRTF is similar to using a phased array transducer for finding the location of the sound source based on the time and amplitude difference between each signal received by different elements across the array. However, there is no equivalent of an asymmetrical spatial filter used in ultrasound localization or imaging. In order to break the surface symmetry and allow 3-D spatial encoding, our design implements the *helix* and *antihelix* shapes, which are the most significant features of the outer ear used for 3-D ear recognition and generating pinna-related transfer functions.

## DESIGN OF THE ACOUSTIC LENS

First, an acoustic lens with a *helix* was designed using a single spiral (a Parker spiral with a  $2\pi$ -turn) shaped mask, as shown in Figure S1 (middle-left). In order to implement the *antihelix* shape, a secondary spiral was inserted to create a dual spiral-shaped mask, as shown in Figure S1 (middle-right) and (right). During the design process, two parameters were tuned: spiral thickness and angular separation between spirals. The separation between spirals were varied between  $0^\circ$  and  $180^\circ$  by rotating the second spiral, where the  $0^\circ$  separation corresponded to a single spiral. Figure S1 (top) shows the dual spiral-shaped mask design, where only spirals with  $0^\circ$ ,  $90^\circ$  and  $180^\circ$  separations were shown for clarity. Thickness values between  $\lambda/8$  and  $\lambda$  were tested.

The design verification was performed using the Field II simulation toolbox in Matlab using a custom solver based on the Tupholme-Stepanishen method as explained in [4, 5]. A single element transducer of 6-mm diameter working at 2.4 MHz was chosen. The receive characteristics of the spiral masks were simulated for mirrored scatterers, such as scatterers located at  $(r, \theta, \varphi)$  and  $(r, \theta, \varphi+180^\circ)$  or  $(r, \theta, \varphi\pm 90^\circ)$ , which would generate identical echo signals without using the proposed method as illustrated in Figure 1 in the main manuscript. To achieve this, scatterers located at  $(2, 2, 40)$ ,  $(2, -2, 40)$ ,  $(-2, 2, 40)$  and  $(-2, -2, 40)$  mm in x-y-z Cartesian coordinates were simulated individually, which corresponded to 4 scatterers located at  $r = 40.1$  mm and  $\theta = 4.05^\circ$  with a varying azimuthal angle of  $\varphi = 45^\circ, 135^\circ, 225^\circ$  and  $315^\circ$  in spherical coordinates. The surfaces of acoustic lenses, which were in contact with the ultrasound transducer, were centered at  $(0, 0, 0)$  mm around the z axis, where positive directions of x and y axes are shown in Figure 2 in the main manuscript.

The simulated transducer consisted of 4197 sub-elements with a size of  $\lambda/8$ , where some of the sub-elements were disabled to simulate the partially blocked ultrasound waves by the designed masks, as shown in Figure S1 (bottom). Each sub-element of the transducer was created using `xdc_2d_array()` function with a center frequency of 2.4 MHz, bandwidth of 60%, which corresponded to 1.44 MHz, width of  $\lambda/8$ , height of  $\lambda/8$  and kerf

of 0 without any focusing. The transducer aperture was defined with rigid-baffle boundary conditions. The impulse response was generated using the Matlab `gauspuls()` function with the aforementioned frequency and bandwidth values and a 40 dB cut-off. The speed of sound was chosen as 1482 m/s to align with experiments performed in water at 20°C. A sampling frequency of 48 MHz, which is 20 fold larger than the center frequency of the transducer, was used. Frequency dependent attenuation was enabled in simulations. After defining the simulation variables, `calc_scatter_multi()` function was used to calculate the received signal reflected from scatterers, where the location of scatterers are given in the main text. The received data were directly plotted without any filtering or further processing. The spectra of the received signals were calculated using the `fft()` function in Matlab.

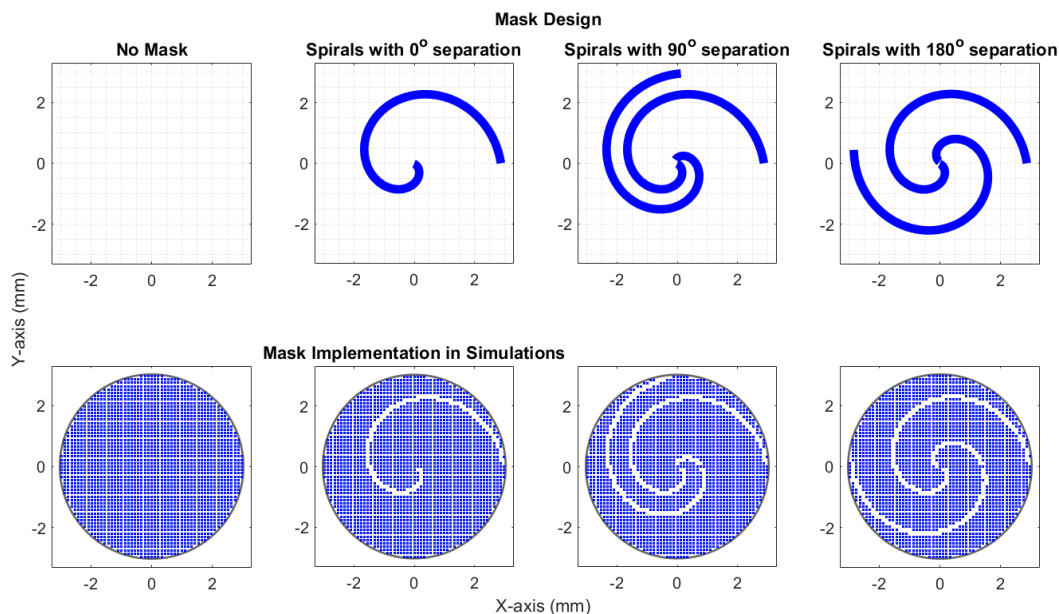


**Fig. S1.** (Top) Different acoustic lens designs with no mask, a single spiral-shaped mask, a dual spiral-shaped mask with 90° separation and a dual spiral-shaped mask with 180° separation. (Bottom) Spiral-shaped masks are implemented in Filed II by partially blocking the transducer's active aperture. Small blue squares represent the active area of the transducer on the simulation grid.

## EVALUATION OF THE SPATIAL ENCODING ACHIEVED BY THE ACOUSTIC LENS

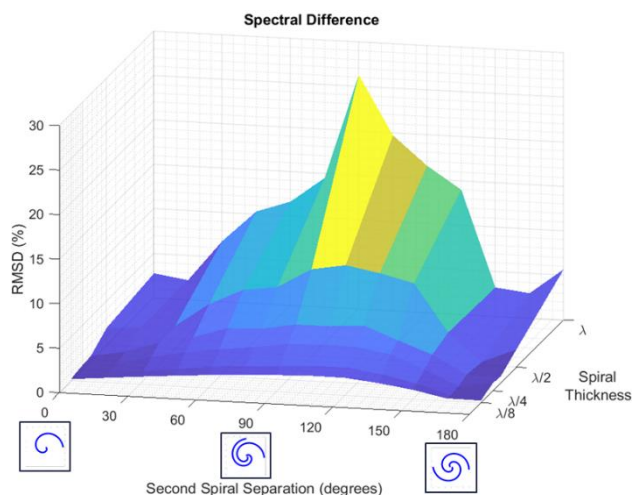


**Fig. S2.** Spectral differences (in percentages) between the echoes of mirrored scatterers are plotted for different mask designs with varying spiral thicknesses and separations.

To evaluate the spatial encoding achieved by different designs, the frequency spectra of received signals were compared with a reference transducer with no mask (see Figure S1 (left)). The spectral difference between signals was evaluated by using the root-mean-square deviation (RMSD) method (also called root-mean-square error). First, all signal spectra were intensity normalized to avoid any differences due to attenuation or the existence of strong/weak scatterers. The RMSD method was then applied by subtracting both signals' spectral amplitudes, squaring them, summing the squared difference values across the whole frequency range, and performing a square root operation. The final results were normalized by the sum of the total spectral

power and multiplied by 100 to find the percentage spectral difference between signals. As shown in Figure S2, a 90° spiral separation and thicker spirals enabled a larger difference in the received signal spectrum for two mirrored scatterers at (2, -2, 40) and (-2, 2, 40), where a larger RMSD means a better encoded signal and hence a lower ambiguity in localization.

## EVALUATION OF THE TRANSMITTED SIGNALS THROUGH THE ACOUSTIC LENS

Although thicker spiral masks provide a better encoding, they also block a larger section of the transducer and reduce receive sensitivity. For a transducer with a dual spiral mask (90° spiral separation), the ultrasound beam profile was simulated with different spiral thicknesses between  $\lambda/8$  and  $\lambda$ , as shown in Figure S3. When the thickness of the dual spiral mask becomes comparable to the ultrasound wavelength ( $>\lambda/4$ ), the hallow mask distorted the transmitted ultrasound field. These distortions create blind spots in the transducer's far field and reduce the detection capabilities of the proposed method, as seen in Figure S3 for the  $\lambda$  spiral thickness at around 10-15 mm depth. The spiral-shaped mask placed in the near-field of the transducer have a negligible effect in the far-field for thickness values  $\leq \lambda/4$ . This phenomenon is explained by Born approximation for ultrasound propagation, where the scattered field is small compared to the incident field for the mask with sub-wavelength features. Therefore, the dual spiral mask with a thickness of  $\lambda/4$  and spiral separation of 90° achieved the best trade-off between received signal encoding and an undistorted transmitted beam shape.

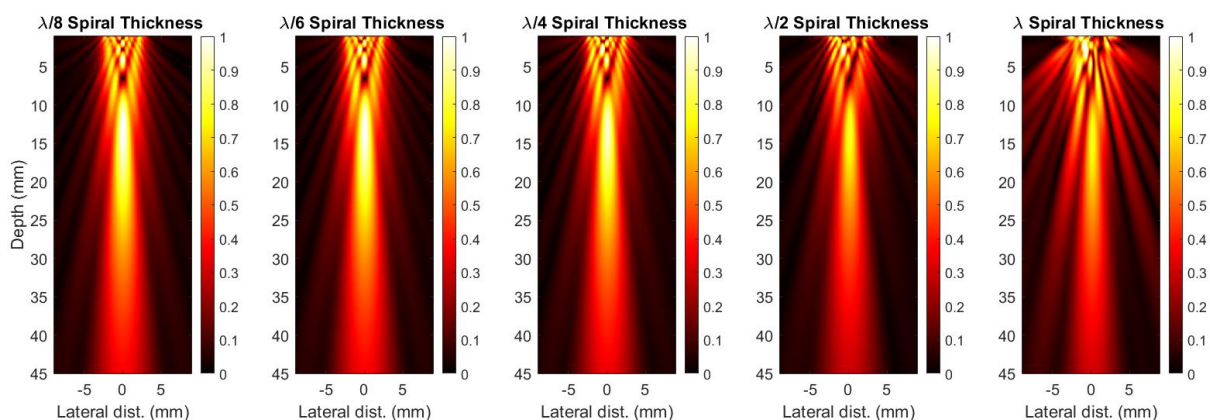


**Fig. S3.** Ultrasound fields radiated from the transducer through a dual spiral-shaped mask (90° spiral separation) with varying spiral thickness values. The x-z cross-sectional view is shown.

## EXPERIMENTAL SETUP WITH THE ACOUSTIC LENS

For the experimental work, HEUT prototypes were built using a single-element transducer and different acoustic lenses with spiral-shaped hallow masks, which were placed in contact with the transducer to block part of the transducer's active surface. The flat side of the lenses was attached to the transducer surface with ultrasound gel in between, and the grooves were filled with air by sealing them with Mylar film. An Ultrasound Array Research Platform (UARP) [6] was programmed to send ultrasound signals and receive the reflected echoes using these HEUT prototypes. Several measurements were performed with each HEUT prototype by re-locating scatterers as explained in the main manuscript. At each location, pulse-echo measurements were repeated for 100 times to improve the signal-to-noise ratio, which varied between 38 and 51 dB for different scatterer locations.

## REFERENCES

- [1] M. M. Van Wanrooij, and A. J. V. Opstal, "Contribution of Head Shadow and Pinna Cues to Chronic Monaural Sound Localization", *Journal of Neuroscience*, vol. 24, no. 17, pp. 4163-4171, 2004.
- [2] S. Mattes, P. Nelson, F. M. Fazi et al. "Towards A Human Perceptual Model for 3D Sound Localization", *Proceedings of the Institute of Acoustics*, vol. 34, 2012.
- [3] V. Best and S. Carlile, "The role of high frequencies in speech localization", *The Journal of the Acoustical Society of America*, vol. 118, pp. 353-363, 2005.
- [4] J. A. Jensen and N. B. Svendsen, "Calculation of pressure fields from arbitrarily shaped apodized and excited ultrasound transducers", *IEEE Trans. Ultrason., Ferroelectr., Freq. Control*, vol. 39, no. 2, pp. 262-267, 1992.
- [5] J. A. Jensen, "Field: A program for simulating ultrasound systems", *10th Nordicbaltic Conference On Biomedical Imaging*, vol. 4, no. 1, pp. 351-353, 1996.
- [6] E. Boni, A. C. H. Yu, S. Freear et al. "Ultrasound Open Platforms for Next-Generation Imaging Technique Development," *IEEE Trans. Ultrason., Ferroelectr., Freq. Control*, vol. 65, no. 7, pp. 1078-1092, 2018